Indian Journal of Chemical Technology
Vol. 31, May 2024, pp. 506-520
DOI: 10.56042/ijct.v31i3.3324

Photocatalytic degradation of organic compounds in dye wastewater by Fe^{3+} doped nano-ZnO/TiO_2 composite photocatalyst

Lin Lin & Khozema Ahmed Ali*
Environmental Technology Division, School of Industrial Technology, Universiti Sains Malaysia, Penang 11800, Malaysia
*E-mail: khozema@usm.my

Received 28 June 2023; accepted 3 April 2024

In this study, a Fe^{3+} doped ZnO/TiO_2 photocatalyst with optimized photocatalytic efficiency has been prepared using the calcination method. The synthesized photocatalyst has been comprehensively characterized using four analytical techniques: X-ray diffraction (XRD), scanning electron microscopy (SEM), energy-dispersive X-ray spectroscopy (EDS), and X-ray photoelectron spectroscopy (XPS). XRD analysis revealed the presence of TiO_2, ZnO, Fe_2O_3, and carbon in the photocatalyst composition. SEM imaging demonstrated that the particle size of the synthesized photocatalyst is at the nanometer scale. EDS results confirmed the successful doping of Fe^{3+} into the photocatalyst structure, with the photocatalyst surface exhibiting carbon enrichment. XPS analysis indicated that the combination of ZnO and TiO_2 promoted the formation of oxygen vacancies on the TiO_2 surface, thereby enhancing photocatalytic efficiency. Optimization experiments revealed that the best photocatalytic performance was achieved when the ratio of Zn $(CH_3COO)_2$, $TiCl_4$, $FeCl_3 \cdot 6H_2O$, and oleic acid was 1:1:0.02:3, with a calcination temperature of 400 °C. Under these conditions, the Fe^{3+} doped ZnO/TiO_2 photocatalyst exhibited superior photocatalytic efficiency. With the addition of 0.2 wt % Fe^{3+} to the ZnO/TiO_2 photocatalyst, the removal rates of methyl orange reached 90.68% and 97.14% after 4 h of exposure to incandescent lamp and sunlight, respectively.

Keywords: Calcination method, Fe^{3+} doped nano-ZnO/TiO_2 composite, Methyl orange degradation, Nano-ZnO/TiO_2 photocatalyst, Visible light photocatalysis

Introduction

The textile industry is advancing rapidly, resulting in increasingly severe pollution of dye wastewater[1, 2]. Azo dyes (-N=N-) are particularly concerning as they are harmful organic substances capable of altering the DNA structure of the human body upon activation, leading to pathological changes and potentially cancerous effects[3]. Recognizing the significant risks associated with azo dyes, various purification methods have been employed, including adsorption, membrane separation, and aerobic/anaerobic treatment technologies[4]. However, compared to these methods, the utilization of photocatalysts for the photocatalytic degradation of azo dyes is imperative. The role of photocatalysts in the photodegradation of dye pollutants is to facilitate the decomposition of dye molecules through photocatalytic reactions. When photocatalysts are exposed to light, they absorb photons and generate excited electrons, creating electron-hole pairs. These excited electrons can participate in redox reactions with water or oxygen molecules. During the degradation of dye pollutants, the photocatalyst's excited electrons react with dye molecules, breaking them down into smaller, harmless substances such as water and carbon dioxide[5, 6].

Firstly, as a typical advanced oxidation technology, adding photocatalyst can quickly and effectively decompose azo dye contaminants without selectivity. Secondly, this method harnesses solar energy as its primary energy source, resulting in minimal environmental impact with no secondary pollution, and only generating water, carbon dioxide (CO_2), and inorganic ions. Thirdly, the photocatalytic reaction process is safe and mild, facilitated by simple devices. Therefore, the implementation of efficient, safe, and environmentally friendly photocatalyst technology holds immense promise for the purification of azo dye wastewater [7].

Numerous experiments have demonstrated the high efficiency of semiconductor photocatalysts, such as TiO_2, ZnO, Fe_2O_3, and CdS, in degrading organic substances under irradiation with light of the appropriate wavelength. Among them, TiO_2 and ZnO have been extensively studied due to their high photocatalytic activity, excellent physical and chemical stability, affordability, and non-toxicity to humans and the environment. However, their practical

application is hindered by the narrow light absorption range (3.2 eV for TiO_2 and 3.37 eV for ZnO) and low charge transfer efficiency, posing significant challenges to their further development. Metal doped nanocomposite material is an ideal photocatalyst for degradation of dyes as it not only possesses the excellent properties of nanomaterials but also harnesses the advantages of metal ions and composite materials.

As a typical N-type semiconductor material, when the grain size of TiO_2 is reduced to the nanometer level, its properties are greatly enhanced. Firstly, nano-TiO_2 can effectively shorten the time of photogenerated carrier migration to the particle surface and decrease the likelihood of carrier recombination within the particles. Secondly, the small particle size of the photocatalyst increases the specific surface area and the number of active sites. Thirdly, the carrier transfer rate at the photoreaction interface is accelerated. Metal ion doping involves incorporating a specific amount of impurity metal ions into the TiO_2 lattice, acting as active "islands". This process profoundly influences the production, recombination, and transfer of electrons and holes, thereby affecting photoactivity. Semiconductor recombination represents a technique to alter the band gap and spectral absorption range of semiconductor photocatalysts by introducing impurity semiconductors[8].

Several studies and experiments have found that the photocatalytic activity and external properties of TiO_2 photocatalyst can be significantly improved if appropriate materials are selected for co-reference hybrid modification. Zielinska-Jurek et al. demonstrated the superior degradation efficiency of phenol using a composite photocatalyst of Ag/Pt/TiO_2, with optimal performance observed at a 0.5% mass fraction of Ag and Pd[9]. Meanwhile, Xie Guixiang et al. synthesized ZnO/C/TiO_2 through a hydrothermal method, achieving an impressive 99.5% degradation rate of methyl orange under ultraviolet light[10]. Additionally, the incorporation of certain metal ions has been found to expand the range of light absorption. In metal ion doped TiO_2 photocatalytic reactions, the capture, release, and migration of holes and electrons within the lattice determine the overall photocatalytic efficiency[11].

This study selected Fe^{3+} as the doping ion and combined it with TiO_2 and ZnO to prepare nano-ZnO/TiO_2 composite photocatalyst. When Fe^{3+} is introduced into TiO_2, several effects occur. Firstly, it narrows the band gap and extends the absorption wavelength into the visible region. Secondly, it increases the excitation of electrons and holes. Thirdly, it reduces electron-hole recombination time, facilitating efficient separation. Moreover, Fe^{3+} doping enhances the adsorption capability of reactants, leading to improved photocatalytic performance. The use of semiconductor material composites not only extends the response of wide-band gap semiconductors but also steers the direction of photogenerated carriers. Combining semiconductors with large and small bandgap energies not only broadens the optical response to visible light but also facilitates the collection and separation of electrons and holes within different particles. Consequently, composite semiconductors often exhibit higher photocatalytic activity than individual semiconductors. At the interface of a ZnO/TiO_2 composite system, the conduction band level of TiO_2 surpasses that of ZnO due to energy band deviations. This results in the formation of a band barrier near the interface, causing electrons to accumulate on the ZnO side. This barrier impedes electron movement, creating a space charge region. The excitation wavelength of TiO_2 spans a wide range. Additionally, carriers separated within the composite semiconductor exhibit prolonged lifetimes, enhancing its quantum efficiency[12].

In this study, a one-step calcination method was used to prepare a nano-ZnO/TiO_2 composite doped with Fe^{3+} ions, followed by a comprehensive characterization. The photocatalytic activity was assessed through degradation experiments under both incandescent lamps and sunlight. The relationship between the variables will be discussed and logically analyzed. The findings of this research could significantly contribute to advancements in photocatalysis and related fields by enhancing the readers understanding of Fe^{3+} doped ZnO/TiO_2 photocatalysts and their potential applications in wastewater treatment and environmental remediation.

Experimental Section

Synthesis and characterization of Fe^{3+} doped ZnO/TiO_2

All chemicals utilized in this study were of analytical grade and distilled water was used throughout. Fe^{3+}doped ZnO/TiO_2 photocatalyst was synthesized by calcination method. $FeCl_3 \cdot 6H_2O$, $Zn(CH_3COO)_2$, $TiCl_4$ and oleic acid were combined in predetermined proportions and distributed into four crucibles[13]. The mixtures were thoroughly stirred with

a glass rod, covered with lids, and heated in a furnace at high temperature. The initial furnace temperature was at room temperature, with a heating rate of 3.125 °C/min. After reaching 400 °C, the temperature was maintained for 6 h. Upon natural cooling, the crucibles were removed, and the resulting samples appeared black[14]. Following grinding into powder, the samples were weighed and transferred into sample bottles. To optimize photocatalyst activity, three factors including the amount of oleic acid and $FeCl_3 \cdot 6H_2O$, as well as the calcination temperature, were separately optimized using control variable methods. The specific quantities of variables are detailed in Table 1.

The photocatalysts underwent characterization through scanning electron microscopy (SEM), energy dispersive spectroscopy (EDS), X-ray photoelectron spectroscopy (XPS), and X-ray diffraction (XRD). SEM was employed to observe and confirm the morphology and particle size of the photocatalysts, while EDS analyzed the elemental composition. XPS provided qualitative insights into the surface elements' composition, chemical states, and molecular structures. XRD facilitated both qualitative and quantitative analyses of the phase composition of the photocatalyst.

Photocatalytic degradation experiments

Methyl orange was chosen as the representative dye pollutant for this study. Initially, the photocatalysts, prepared under various conditions (including oleic acid amount, Fe^{3+} amount, and calcination temperature), were added to a 20 mg/L methyl orange solution. The mixture was then subjected to photocatalytic degradation experiments under a 100 W incandescent lamp (providing visible light). After each designated time interval (0.5 h, 1 h, 2 h, 3 h, and 4 h), the absorbance of methyl orange was measured. Subsequently, the concentration of methyl orange corresponding to the absorbance was determined using Lambert Beer's law and a standard curve.

The removal of methyl orange comprises two components. On one side, under light conditions, methyl orange undergoes oxidation, decomposing into CO_2, water molecules, and other by-products. On the other side, some methyl orange molecules are adsorbed onto the surface of the photocatalyst. Therefore, in order to accurately quantify the amount of methyl orange degraded and physically adsorbed by the prepared photocatalysts, desorption tests were conducted[15]. Following the 4-h photocatalytic degradation experiment, the solution obtained was cooled to room temperature and filtered to isolate the photocatalysts. Subsequently, the photocatalyst was dried at room temperature and transferred into a 100 mL beaker. Distilled water (100 mL) was then added to the beaker. The beaker was subjected to ultrasonication for five minutes, during which the methyl orange molecules on the photocatalyst's surface were dislodged into the distilled water. By measuring the absorbance of the distilled water after ultrasonication, the quantity of methyl orange adsorbed on the photocatalyst's surface could be determined. Finally, the amount of methyl orange decomposed by the photocatalyst was calculated.

Photocatalytic degradation experiments under sunlight

To determine whether the absorption wavelength range of the prepared photocatalyst extended to the ultraviolet range, photocatalytic degradation experiments under sunlight were conducted. Sunlight, with its broader spectrum including visible and ultraviolet light, provides a comprehensive assessment. This approach also allows for comparison between the light sources of an incandescent lamp and sunlight. Experimental procedures mirrored those of the photocatalytic experiments under a 100 W incandescent lamp, with the sole difference being the substitution of the incandescent lamp with sunlight[16].

Photocatalytic experiments with different photocatalyst doses

Initially, three 100 mL solutions of methyl orange with a concentration of 20 mg/L were individually poured into three 100 mL beakers. Subsequently, 0.1 g, 0.4 g, and 0.6 g of the measured photocatalyst were respectively added to the beakers. Following labelling, the three beakers were simultaneously

Table 1 — Exact quantities of three factors

Factors	$Zn(CH_3COO)_2$: $TiCl_4$: $FeCl_3 \cdot 6H_2O$: Oleic acid					
Oleic acid	1: 1: 0.01: 2		1: 1: 0.01: 2.5	1: 1: 0.01: 3		1: 1: 0.01: 4
$FeCl_3 \cdot 6H_2O$	1: 1: 0.02: X		1: 1: 0.03: X	1: 1: 0.04: X		1: 1: 0.05: X
Calcination temperature (°C)	350	400	450	500	550	600

(Note: X = 3 after optimization of oleic acid)

positioned under a 100 W incandescent lamp for exposure. Sequentially, absorbance readings were taken at intervals of 0.5 h, 1 h, 2 h, 3 h, and 4 h, and the corresponding methyl orange concentrations were determined using Lambert Beer's law and the standard curve. Finally, the removal rate was computed.

Results and Discussion

Photocatalyst characterization

SEM analysis

Figs 1(a) and 1(b) depict SEM images of the nano Fe^{3+}doped ZnO/TiO_2 composite photocatalyst prepared under optimal oleic acid conditions. In these

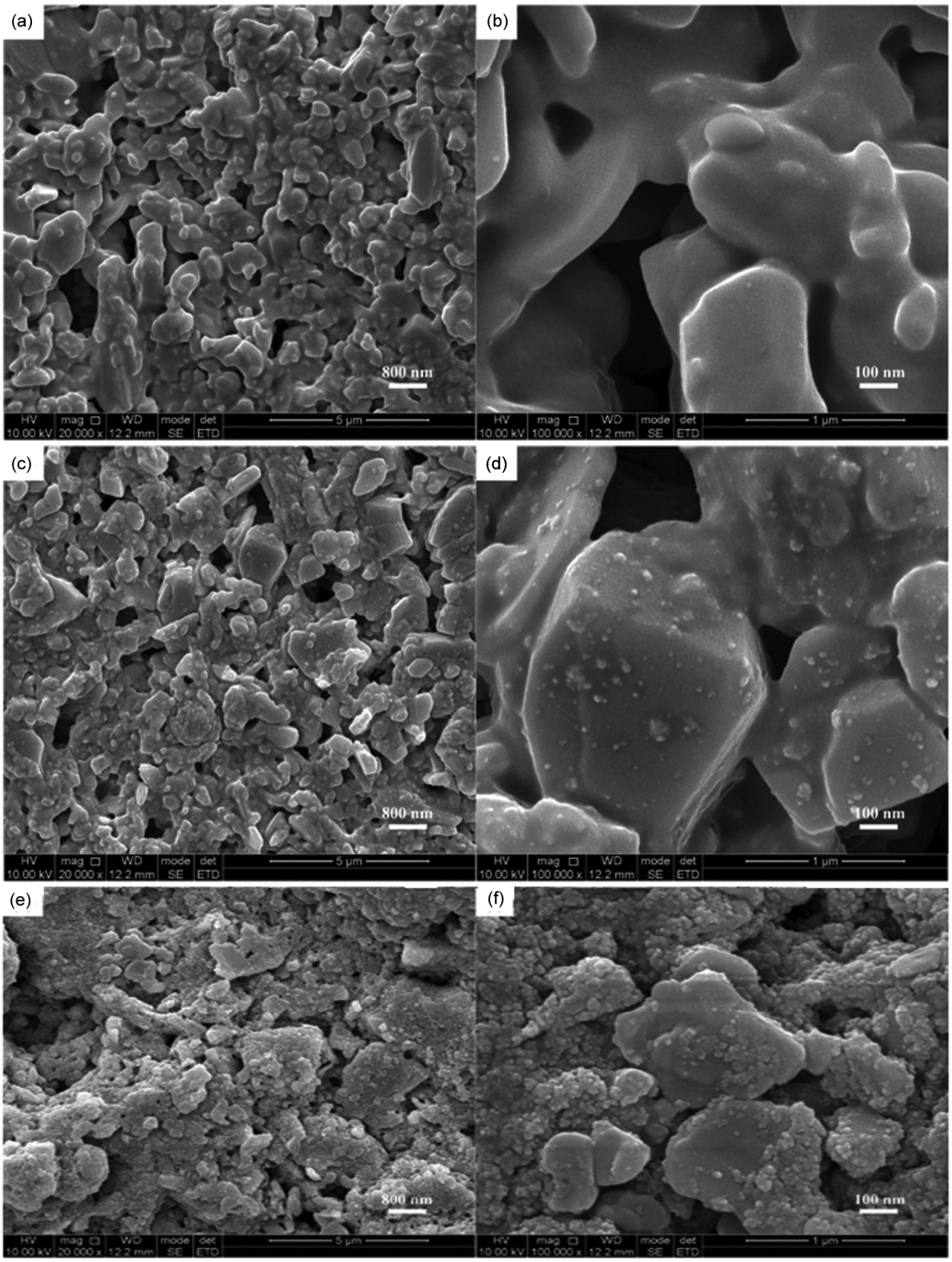

Fig. 1 — SEM images of 0.2 wt% Fe^{3+} doped ZnO/TiO_2 composite photocatalyst with (a) & (b) optimization of oleic acid, (c) & (d) optimization of $FeCl_3 \cdot 6H_2O$, (e) & (f) optimization of temperature

images, it can be observed that the sample is primarily composed of highly aggregated spherical particles. Based on the scale, it can be roughly estimated that the particle sizes are mainly concentrated between 200 nm and 800 nm, reaching the nanoscale, with relatively uniform dispersion and a large surface area. Additionally, smaller particles with a diameter of approximately 100 nm are observed deposited on the surface of larger particles, attributed to the optimization of Fe^{3+}. Furthermore, a minor aggregation phenomenon, known as agglomeration, is visible in some parts of the sample, likely due to inappropriate heating rates and temperatures during the reaction, among other reasons[17].

Figs 1(c) and 1(d) display SEM images of the nano Fe^{3+}doped ZnO/TiO_2 composite photocatalyst prepared under optimal oleic acid and $FeCl_3 \cdot 6H_2O$ conditions. A comparison between Figs 1(a) and 1(c) reveals a more pronounced aggregation of nanoparticles, with irregular nano-sized particles appearing on the surface, resulting in fragmented spherical structures and a rough surface. Moreover, a notable difference in the microstructure of the samples before and after optimizing the $FeCl_3 \cdot 6H_2O$ addition is observed from the comparison between Figs 1(d) and 1(b). The disappearance of larger diameter particles from the sample surface and the presence of numerous small particles with diameters ranging from 1-10 nm are evident. This is attributed to the successful doping of transition metal Fe^{3+} into nano ZnO/TiO_2, reaching an optimal state. The smaller radius of Fe^{3+} compared to the crystal sizes of nano ZnO and TiO_2 results in the occupancy of internal spaces within the nanostructures, leading to defects and dislocations, distortion of the nano ZnO and TiO_2 crystals, and disruption of the original crystalline characteristics. Similar conclusions have been confirmed in studies on transition metal doped ZnO and TiO_2 modification.

Figs 1(e) and 1(f) depict SEM images of the Fe^{3+}doped ZnO/TiO_2 composite photocatalyst prepared under optimal conditions, i.e., with optimal oleic acid and $FeCl_3 \cdot 6H_2O$ concentration, and at the optimal temperature. The photocatalyst was prepared using calcination method with zinc acetate, titanium tetrachloride, oleic acid, and ferric chloride hexahydrate as reactants. Based on the images, the particle sizes are mainly concentrated between 35 nm and 88 nm. It can also be observed that the nanoparticles prepared under optimal conditions are much smaller compared to those in the other two states, with more uniform distribution and smaller particle size across most areas, resulting in a larger surface area, achieving an even smaller nano-scale level.

EDS analysis

The EDS analysis revealed qualitative and quantitative information about the sample's elemental composition. EDS analysis was conducted on three parts of the sample, showing slight deviations in the elemental content among them, albeit maintaining consistent elemental rankings. The spectra analysis (Fig. 2 and Table 2) confirmed the presence of carbon (C), oxygen (O), titanium (Ti), iron (Fe), and zinc (Zn) in the sample. Notably, carbon had the highest content, followed by Zn, O, Ti, and Fe, with Fe having the lowest concentration. The successful presence of Fe indicated its effective doping into the photocatalyst structure without impurities. The predominant presence of carbon resulted in a black appearance on the sample surface, attributed to its highest content. Given the synthesis process of the photocatalyst, oleic acid serves as the source of carbon. Further desorption experiments corroborated the physical adsorption of carbon elements onto the photocatalyst surface[18].

XPS analysis

XPS characterization analyzes the electronic states and binding energies of elements in the sample. Fig. 3 presents the XPS spectra of the photocatalyst prepared under optimal conditions. Fig. 3(a) displays the full spectrum of the composite photocatalyst sample, indicating the presence of five elements: Zn, C, O, Ti, and Fe. Fig. 3(b) shows the high-resolution spectrum of Zn2p, whose distinct peaks appear at 1046.35 eV (Zn $2p_{1/2}$) and 1023.12 eV (Zn $2p_{3/2}$), with a difference of 23.23 eV. This difference closely matches the standard binding energy difference of Zn^{2+} (23.2 eV), suggesting that most of the Zn in the sample exists in the form of Zn^{2+} and aligns with the binding energy data of nano-ZnO. Fig. 3(c) presents the high-resolution spectrum of C1s obtained by calibrating the element peaks using C1s as the standard peak binding energy (284.80 eV). Fig. 3(d) shows the high-resolution spectrum of O1s obtained by calibrating the element peaks using O1s as the standard peak binding energy (530 eV). The peak on the right is located near the binding energy of 533 eV, typically associated with oxides or oxygen-containing functional groups. Considering the preparation process of the photocatalyst through the calcination method, it is speculated that during the sample calcination, oleic

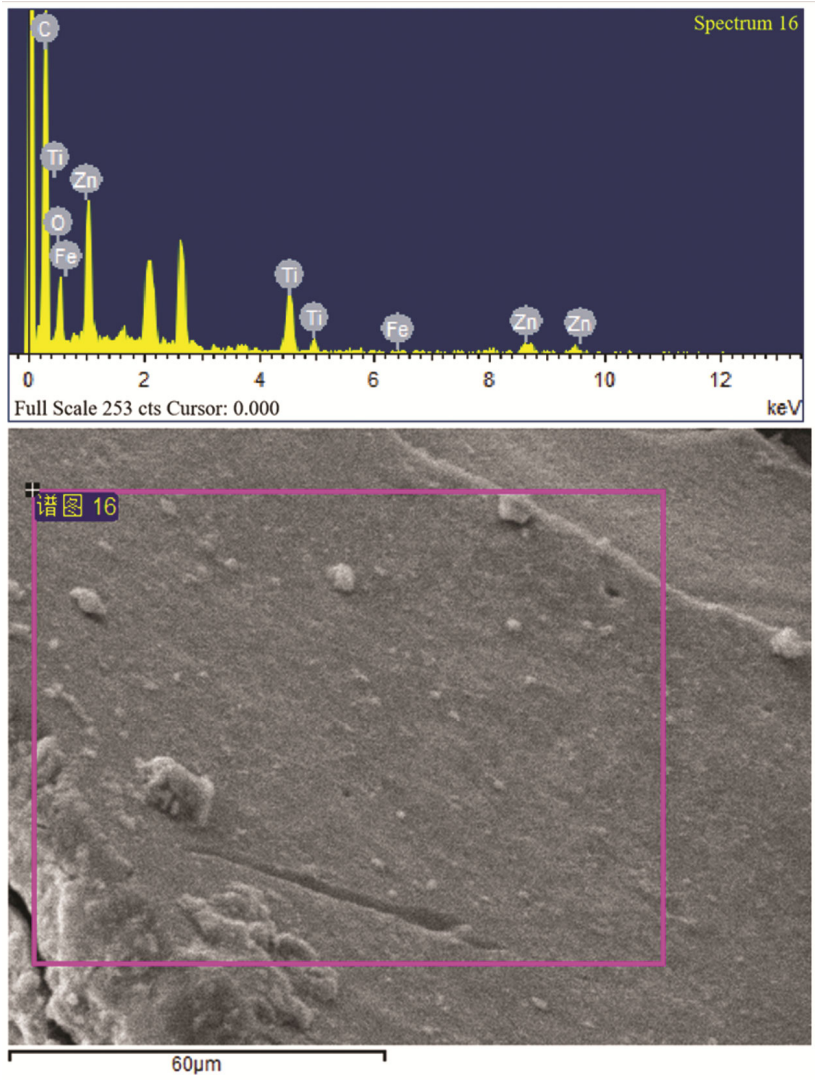

Fig. 2 — EDS analysis of 0.2 wt% Fe^{3+} doped ZnO/TiO_2 composite photocatalyst

Table 2 — EDS analysis of 0.2 wt% Fe^{3+} doped ZnO/TiO_2 composite photocatalyst

Element	Weight %	Atomic %
C K	61.30	78.02
O K	16.94	16.19
Ti K	7.98	2.55
Fe K	0.59	0.16
Zn L	13.18	3.08
Total	100.00	100.00

acid is converted into carbon nanotubes, which coat the surface of the photocatalyst and combine with oxygen to generate C=O and C-O. Further analysis is required to determine the specific chemical substances represented by the peak near O 533 eV. Fig. 3(e) presents the high-resolution spectrum of Ti2p, with peaks at 458.41 eV and 464.53 eV corresponding to the binding energies of $Ti2p_{3/2}$ and $Ti2p_{1/2}$, respectively. Figs 3(f) and (g) show the high-resolution spectra of Fe2p. However, due to the low doping level of Fe^{3+} (0.2 wt%), the spectra exhibit significant fluctuations. After fitting, distinct peaks appear at 705.83 eV and 719.17 eV, corresponding to $Fe2p_{3/2}$ and $Fe2p_{1/2}$. Additionally, peaks appear at 712.70 eV and 728.33 eV, which closely match the standard binding energies of Fe^{3+} (710.7 eV and 724.3 eV), indicating that some iron exists in the form of Fe^{3+} within the nano-ZnO/TiO_2, rather than distributed on the surface of the material. Finally, some impurity peaks are observed in the spectra, possibly indicating the presence of other forms of Fe. The preparation of the nano-ZnO/TiO_2 composite photocatalyst increases the oxygen vacancies on the surface of TiO_2 due to the presence of

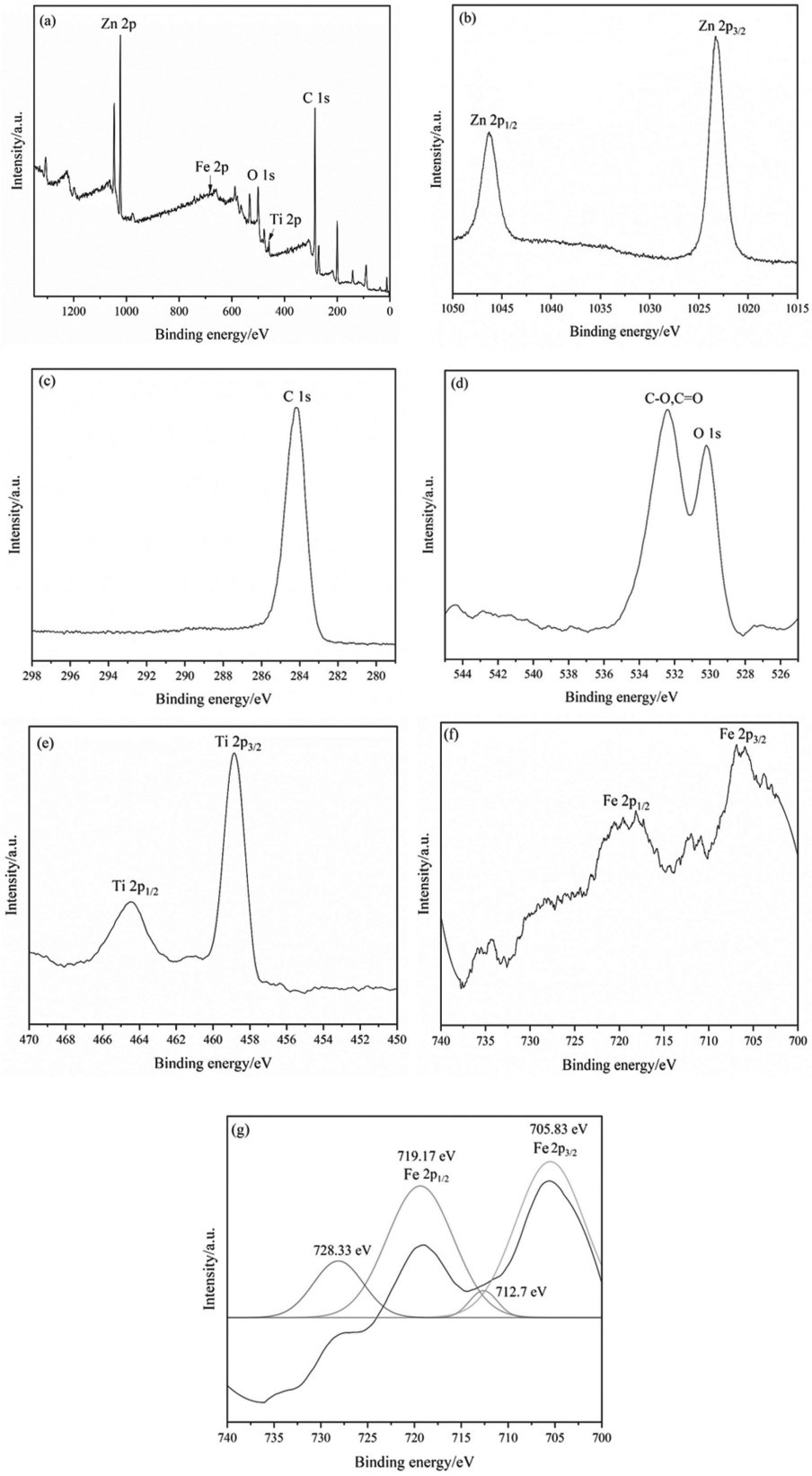

Fig. 3 — XPS spectra of 0.2 wt% Fe^{3+} doped ZnO/TiO_2 composite photocatalyst: (a) Full XPS survey spectrum, (b) Zn 2p, (c) C 1s, (d) O ls, (e) Ti 2p, (f) and (g) Fe spectra

ZnO, consequently reducing the content of free electrons. Moreover, the increase in oxygen vacancy content on the photocatalyst surface facilitates oxygen molecule adsorption, thereby enhancing the photocatalytic efficiency of the photocatalyst[18, 19].

XRD analysis

Fig. 4 illustrates the XRD pattern of the optimized photocatalyst, analyzed using JADE software. The diffraction peaks of TiO_2 in the sample coincide with those of the TiO_2 standard PDF card (JCPDSNo.21-1272). Specifically, the diffraction angles 2θ = 25.3°, 37.8°, 48.1°, 53.9°, 68.8°, and 75.1° correspond to the crystal planes of (101), (004), (200), (105), (116), and (215) of the wurtzite phase, respectively. The sharp diffraction peaks in the figure indicate high intensity and good crystallinity. The level of crystallinity in the photocatalyst can impact its surface area, as higher crystallinity may result in a reduction of surface area. Thus, achieving both a large surface area and high crystallinity requires precise temperature control during sample preparation[20]. Similarly, the diffraction peak of ZnO in the sample aligns with the ZnO standard PDF card (JCPDSNo.36-1451). The diffraction angles 2θ = 31.8°, 34.4°, 36.3°, and 62.9° correspond to the crystal planes of (002), (101), and (103) of the hexagonal wurtzite phase, respectively. Compared to TiO_2, the diffraction peaks for ZnO in the figure are less sharp and intense, possibly due to lower purity of ZnO nanoparticles compared to TiO_2. Alternatively, lower TiO_2 content in the sample or uneven sampling may also contribute to this difference. Furthermore, the diffraction peaks of Fe_2O_3 in the sample match those of the standard PDF card of Fe_2O_3 (JCPDSNo.47-1109). The diffraction angles 2θ = 33.16° and 84.95° correspond to the crystal planes of (104) and (124) hematite phase, respectively. Additionally, the green-marked peak represents the diffraction peaks of carbon, aligning with the carbon standard PDF card (JCPDSNo.46-0943). The diffraction angle 2θ=56.00° corresponds to the (107) crystal plane of carbon[21]. The % crystallinity, lattice spacing, lattice constant and average crystallite size are found to be 51.40%, 0.22 mm, 0.386 and 14.51 nm, respectively, using full spectrum fitting method and Scherrer formula to the XRD results.

The crystallite size of 0.2 wt% Fe^{3+} doped ZnO/TiO_2 composite photocatalyst is calculated to be 14.51 nm, which is consistent with the particle diameters of between 35 nm and 88 nm obtained by SEM. SEM is mainly used to observe the surface morphology and microstructure of sample particles, but it can't provide detailed information about crystal structure and crystallite size, so its measurements are often based on approximate estimations of surface morphology. XRD is used to determine the crystal structure and lattice parameters of crystals, including grain size, lattice spacing, etc. It analyzes the crystal structure of the sample by measuring the diffraction patterns of crystals to incident X-rays, providing more accurate crystal parameters, especially grain size. The number of grains in a nano TiO_2 particle can vary depending on preparation conditions, treatment methods, and the specific morphology of the material. In general, nano TiO_2 particles may contain multiple grains inside, which form grain boundaries in the material's crystal structure. The specific number of grains depends on factors such as the size, shape, crystal structure of nano TiO_2 particles, and parameters during preparation. In typical cases, nano TiO_2 particles may contain several to dozens of grains.

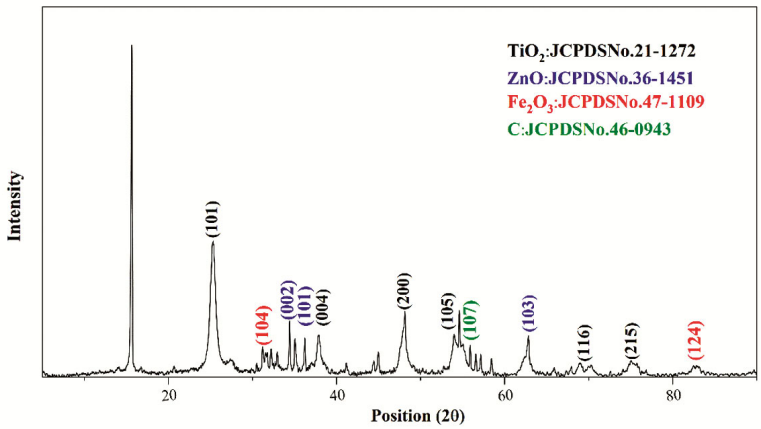

Fig. 4 — X-ray diffractogram of 0.2 wt% Fe^{3+} doped ZnO/TiO_2 composite photocatalyst

Optimization of oleic acid

In this section, to determine the optimal ratio of oleic acid, four photocatalysts were prepared with oleic acid as the sole variable (Table 3). These photocatalysts, produced with varying dosages, underwent three experiments (Fig. 5). The photocatalysts prepared with different dosages were tested by three experiments (Fig. 5). From the results, it can be known that the photocatalytic efficiency of Group C is the best. What's more, the photocatalytic efficiency of the photocatalyst is 6-7% higher under sunlight than under 100 W incandescent lamp, which may be due to the ultraviolet response of the photocatalyst. Firstly, concerning spectral distribution, sunlight covers a broader spectrum including the entire visible light spectrum and ultraviolet radiation, whereas incandescent lamps primarily emit visible light with a relatively narrow range of spectral distribution. Photocatalytic reactions typically require ultraviolet light to excite the active centers of photocatalysts, thus the richer ultraviolet component in sunlight can more effectively stimulate the activity of photocatalysts, enhancing reaction efficiency. Secondly, in terms of intensity, sunlight generally has a much higher intensity compared to an incandescent lamp, meaning that photocatalysts receive more illumination within the same timeframe, thereby promoting the progress of photocatalytic reactions. Higher light intensity can increase the light absorption rate and photocatalytic reaction rate on the surface of photocatalysts, thereby improving photocatalytic efficiency. Thirdly, regarding wavelength adaptability, the spectrum of sunlight is better suited for the absorption and excitation of photocatalysts as it covers a wider range of wavelengths including ultraviolet and visible light. In contrast, the spectrum of incandescent lamps is mainly concentrated in the visible light region, with fewer ultraviolet components that may not effectively excite the activity of photocatalysts. In conclusion, due to the broader spectral range, higher intensity, and better wavelength adaptability of sunlight, photocatalysts typically exhibit superior performance under sunlight compared to under a 100 W incandescent lamp[22].

From the results of desorption tests of methyl orange, it can be known that the photocatalyst prepared not only has the function of chemical

Table 3 — Optimization of photocatalysts through different oleic acid amount

Substance	A	B	C	D
Oleic acid	6.34 mL (20 mmol)	7.93 mL (25 mmol)	9.51 mL (30 mmol)	12.68 mL (40 mmol)
$Zn(CH_3COO)_2$	1.835 g (10 mmol)			
$TiCl_4$	1.10 mL (10 mmol)			
$FeCl_3 \cdot 6H_2O$	0.028 g (0.1 mmol)			
Distilled water	4.00 mL			
Temperature	400 °C			

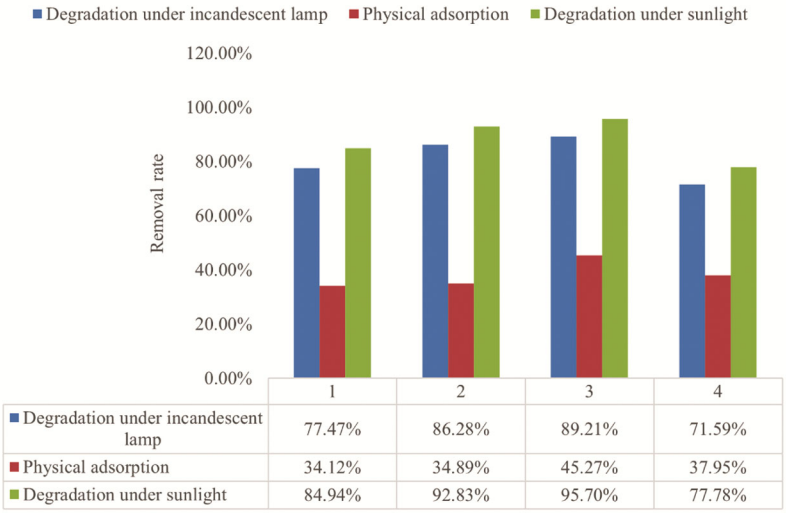

	1	2	3	4
Degradation under incandescent lamp	77.47%	86.28%	89.21%	71.59%
Physical adsorption	34.12%	34.89%	45.27%	37.95%
Degradation under sunlight	84.94%	92.83%	95.70%	77.78%

Fig. 5 — Removal rate of methyl orange for $Fe^{3+}/TiO_2/ZnO$ with different oleic acid concentration under sunlight irradiation and under incandescent light irradiation & physical adsorption of methyl orange on the surface of photocatalyst

degradation of methyl orange, but also has physical adsorption. The amount of adsorption is nearly half under optimal conditions, which may be due to the adsorption of black carbon formed by the photocatalyst. During the experiments, experiments with different doses of photocatalysts were also attempted, showing that the amount of 0.2 g is the optimal amount.

Optimization of $FeCl_3 \cdot 6H_2O$

Based on the experiments optimizing oleic acid, the photocatalytic efficiency was found to be optimal at a ratio of 3 between oleic acid and $TiCl_4$. To determine the ideal ratio of $FeCl_3 \cdot 6H_2O$, four photocatalysts ($TiCl_4$: Fe^{3+} = 1: 0.02, 0.03, 0.04, 0.05) were prepared with $FeCl_3 \cdot 6H_2O$ as the sole variable (Table 4). These photocatalysts were subjected to three experiments (Fig. 6). Analysis of the data reveals that Group B (0.056 g) exhibits the highest photocatalytic efficiency and the lowest absorbance, particularly under sunlight compared to incandescent lamp conditions. These findings indicate that the incorporation of Fe^{3+} enhances the photocatalytic effect. However, as the amount of $FeCl_3 \cdot 6H_2O$ increases, the photocatalytic efficiency diminishes. This may be attributed to the similar radii of iron and titanium ions, leading to iron ions infiltrating the lattice of TiO_2 and replacing titanium ions, thus causing lattice distortion and structural alteration. Consequently, the photocatalytic effect deteriorates with higher concentrations of $FeCl_3 \cdot 6H_2O$.

Optimization of calcination temperature

Based on the experiments optimizing oleic acid and $FeCl_3 \cdot 6H_2O$, the photocatalytic efficiency is highest and optimal when the ratio of oleic acid: $TiCl_4$: $FeCl_3 \cdot 6H_2O$ is 3: 1: 0.02. The purpose of preparing identical photocatalysts with varying calcination temperatures in the same ratio is to explore the influence of temperature on the properties of the photocatalyst, which include its morphology, crystallinity, and photocatalytic activity[23]. To determine the optimal calcination temperature, six identical photocatalysts with the same ratio were prepared as detailed in Table 5. The results (depicted in Fig. 7) show that as the temperature increases, the colour of the photocatalyst becomes lighter and even takes on a reddish hue. It is speculated that the

Table 4 — Optimization of photocatalysts through different $FeCl_3 \cdot 6H_2O$ amount

Substance	A	B	C	D	E
$FeCl_3 \cdot 6H_2O$	0.028 g	0.056 g	0.085 g	0.113 g	0.141 g
$Zn(CH_3COO)_2$	1.835 g (10 mmol)				
$TiCl_4$	1.10 mL (10 mmol)				
Oleic acid	9.51 mL (30 mmol)				
Distilled water	4.00 mL				
Temperature	400 °C				

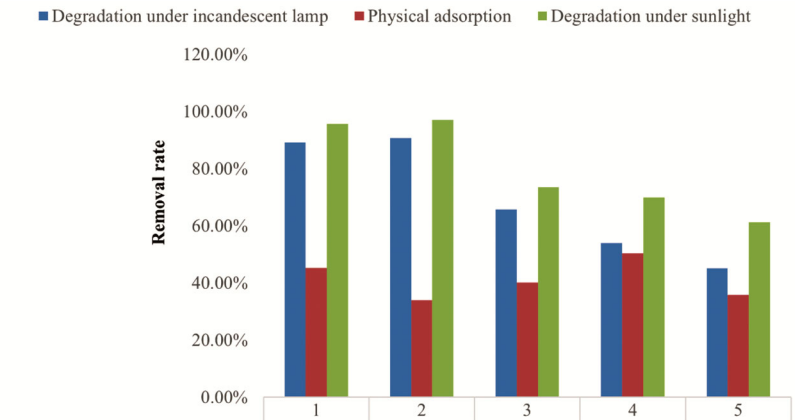

Fig. 6 — Removal rate of methyl orange for Fe^{3+}/TiO_2/ZnO with different $FeCl_3 \cdot 6H_2O$ concentration under sunlight irradiation and under incandescent light irradiation & physical adsorption of methyl orange on the surface of photocatalyst

Table 5 — Optimization of photocatalysts through different reaction temperature

Substance	A	B	C	D	E	F
Temperature	350 ℃	400 ℃	450 ℃	500 ℃	550 ℃	600 ℃
$Zn(CH_3COO)_2$	1.835 g (10 mmol)					
$TiCl_4$	1.10 mL (10 mmol)					
Oleic acid	9.51 mL (30 mmol)					
Distilled water	4.00 mL					
$FeCl_3 \cdot 6H_2O$	0.056 g (0.2 mmol)					

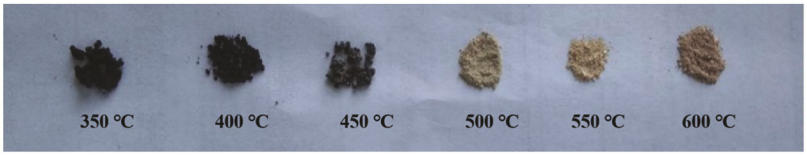

Fig. 7 — Products under six different calcination temperatures

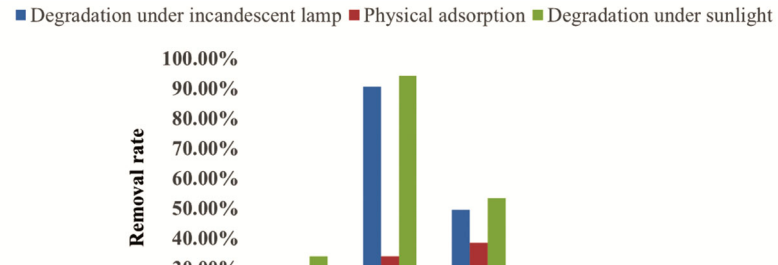

	350 ℃	400 ℃	450 ℃	500 ℃	550 ℃	600 ℃
Degradation under incandescent lamp	18.72%	90.68%	49.56%	9.91%	0	0
Physical adsorption	27.45%	34.00%	38.52%	29.63%	0	0
Degradation under sunlight	34.05%	94.27%	53.41%	26.16%	0	0

Fig. 8 — Removal rate of methyl orange for $Fe^{3+}/TiO_2/ZnO$ with different calcination temperatures under sunlight irradiation and under incandescent light irradiation & physical adsorption of methyl orange on the surface of photocatalyst

photocatalyst's surface is coated with a layer of carbon black. Literature indicates that carbon nanotubes (CNT) remain relatively stable below 500 ℃, and any photocatalysts prepared above this temperature lose their activities due to oxidation reactions. It is hypothesized that during photocatalyst preparation, oleic acid converts into CNT and coats the photocatalyst's surface. The reddish coloration observed in photocatalysts above 500 ℃ may be due to CNT oxidation, along with the presence of red-brown iron oxide solid, resulting in an earth red hue when combined with white ZnO and TiO_2[24]. In this temperature group, the results indicate that at 450 ℃, the photocatalyst exhibits the highest physical adsorption at 38.52%, whereas at 550 ℃ and 600 ℃, no desorption effect is observed. Additionally, the physical adsorption of other groups ranges from 25% to 35%. According to the data, it is evident that photocatalysts synthesized at 400 ℃ still demonstrate the highest photocatalytic efficiency, with slightly better performance under sunlight compared to incandescent light (refer to Fig. 8).

The analysis of the physical adsorption data of all 13 prepared photocatalysts are shown in Table 6 and Fig. 9. From the analysis, it can be observed that, excluding S12 and S13 that exhibited no adsorption capacity, the average adsorption of the other samples is 37.11%. Among these, S7 exhibits the highest physical adsorption performance at 50.34%, while the lowest is observed in S9 at 27.45%. Statistical analysis reveals that among the 11 samples, 5 samples have adsorption values above the average, namely S3, S4, S6, S7, and S10. Interestingly, except for S10, all other four samples have a reaction temperature of 400 ℃. This suggests that reaction temperature significantly influences the physical adsorption

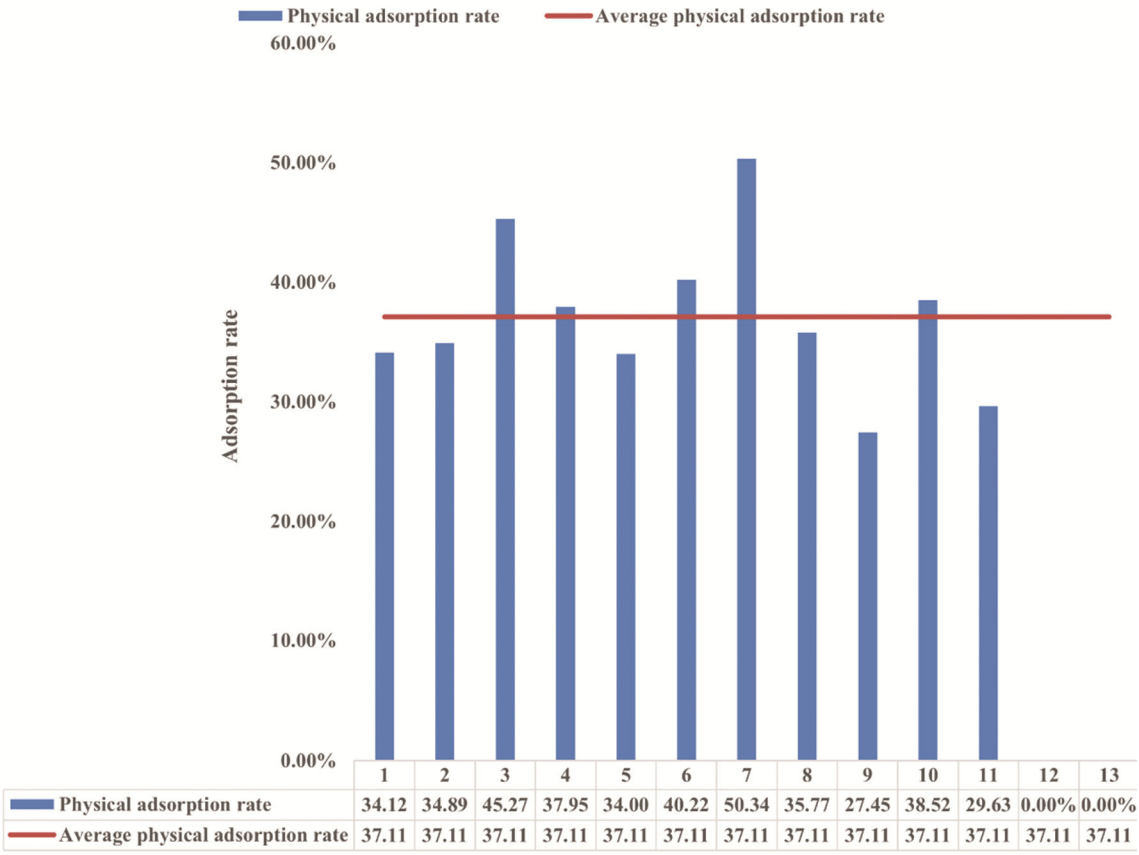

Fig. 9 — Adsorption rate of all the photocatalysts prepared

Table 6 — Adsorption rate of all the photocatalysts

Sample	Oleic acid (mmol)	$Zn(CH_3COO)_2$(mmol)	$TiCl_4$ (mmol)	$FeCl_3 \cdot 6H_2O$ (mmol)	Temperature (°C)	Adsorption rate (%)
S1	2	1	1	0.1	400	34.12
S2	2.5	1	1	0.1	400	34.89
S3	3	1	1	0.1	400	45.27
S4	4	1	1	0.1	400	37.95
S5	3	1	1	0.2	400	34.00
S6	3	1	1	0.3	400	40.22
S7	3	1	1	0.4	400	50.34
S8	3	1	1	0.5	400	35.77
S9	3	1	1	0.2	350	27.45
S10	3	1	1	0.2	450	38.52
S11	3	1	1	0.2	500	29.63
S12	3	1	1	0.2	550	0
S13	3	1	1	0.2	600	0

capacity of the photocatalyst, possibly due to its effect on the carbon layer on the photocatalyst surface.

The carbon on the surface of photocatalysts produced by a muffle furnace typically originates from residual carbon generated during the thermal decomposition or pyrolysis of organic precursor materials. The process of synthesizing photocatalysts involves the use of oleic acid as a solvent, so the source of the carbon layer may be the thermal decomposition or pyrolysis of oleic acid[25]. This carbon often exists in an amorphous or nanoscale particle form on the surface of the photocatalyst. These carbon residues may exert certain effects on the performance of the photocatalyst, depending on the nature of the carbon layer and the specific conditions of the photocatalytic reaction. Its impacts include the following four aspects. Firstly, regarding light absorption properties, the carbon layer can absorb

light and alter the light absorption characteristics of the photocatalyst. It may absorb light within specific wavelength ranges, thus affecting the photocatalyst's light absorption rate and activity. Secondly, concerning the recombination of photogenerated charge carriers, the carbon layer may influence the recombination process of photogenerated charge carriers, thereby affecting the photocatalyst's photocarrier lifetime and efficiency. It may serve as recombination center for electrons and holes, leading to a increase in the recombination rate of electron-hole pairs, thereby reducing photocatalytic activity. Thirdly, regarding the accessibility of reaction centers, the carbon layer may hinder the contact between reactants and the photocatalyst surface, thereby reducing the reaction rate and photocatalytic activity. It may form a barrier layer, reducing the accessibility of active sites. Fourthly, concerning the stability of the photocatalyst, the carbon layer may enhance the stability of the photocatalyst, making it more durable and potentially increasing its stability during the photocatalytic reaction process. However, in some cases, the carbon layer may also cause deactivation or degradation of the photocatalyst[26,27].

Overall, the impact of the carbon layer on the photocatalyst is complex and depends on various factors, including the properties of the carbon layer, specific conditions of the photocatalytic reaction, and properties of the photocatalyst itself. Therefore, in the design and optimization of photocatalysts, it is essential to consider the presence of the carbon layer and its potential effects on catalytic performance.

Upon analysis, it was determined that even after excluding the physical adsorption rate obtained from the control experiment, the photocatalytic efficiency of the optimal photocatalyst (S5) remained superior as shown in Fig. 10. The photocatalytic efficiency of the photocatalyst synthesized at 400 °C may be the highest due to optimal conditions for crystallinity, surface area, and active sites. It was also observed that in the S9 and S11, the physically adsorbed rates of the prepared samples exceeded the overall photocatalytic efficiency. There are several factors contributing to this phenomenon. Firstly, the carbon layer on the photocatalyst's surface may enhance its adsorption capacity. Carbon typically boasts a larger surface area and abundant functional groups, facilitating the adsorption of target molecules. However, this carbon layer could also potentially compromise the accuracy of adsorption rates, especially when employing surface analysis techniques like XPS and SEM. Signal interference or masking due to the carbon layer's presence may affect precise surface composition analysis. Therefore, it's crucial to consider carbon's presence and choose appropriate experimental

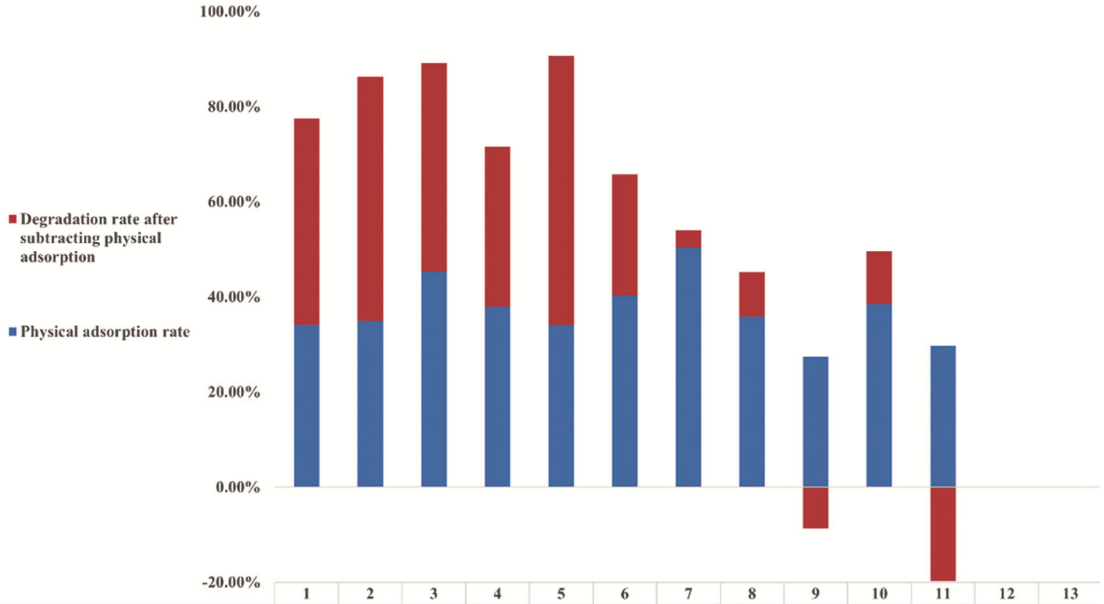

	1	2	3	4	5	6	7	8	9	10	11	12	13
Degradation rate after subtracting physical adsorption	43.35%	51.39%	43.94%	33.64%	56.68%	25.50%	3.63%	9.39%	-8.73%	11.04%	-19.72%	0.00%	0.00%
Physical adsorption rate	34.12%	34.89%	45.27%	37.95%	34.00%	40.22%	50.34%	35.77%	27.45%	38.52%	29.63%	0.00%	0.00%

Fig. 10 — Physical adsorption rate and degradation rate after subtracting physical adsorption

methods when conducting adsorption experiments for accurate results. Secondly, the experimental conditions and methods used in the adsorption experiment might favor more physical adsorption of methyl orange molecules onto the photocatalyst's surface, while photocatalytic degradation efficiency is influenced by additional factors such as light conditions and photocatalyst activity. Thirdly, the adsorption experiment may encompass not only physical adsorption of methyl orange molecules but also other forms like chemical or electrostatic adsorption, potentially inflating the measured adsorption rate. Lastly, the photocatalytic degradation efficiency is sensitive to light conditions such as intensity and illumination time, whereas adsorption experiments often occur under stable conditions, leading to comparatively higher adsorption rates. In summary, the discrepancy between the higher adsorption rate from the experiment and the photocatalytic degradation efficiency may stem from various factors, including experimental conditions, measurement methods, and the influence of carbon during the photocatalytic process[28].

The performance of photocatalysts in dye degradation typically encompasses two primary aspects: physical adsorption and photocatalytic degradation. Physical adsorption refers to the ability of photocatalysts to attract and retain dye molecules on their surfaces. By adsorbing onto the photocatalyst surface, dye molecules establish contact, facilitating subsequent photocatalytic degradation processes. This physical adsorption capability can be modulated through factors such as surface area and pore structure, thereby influencing the adsorption efficiency of photocatalysts. Photocatalytic degradation involves the conversion of light energy by photocatalysts into reactive oxygen species (ROS), such as free radicals or hydroxyl radicals. These ROS then react with and oxidize dye molecules, breaking them down into harmless byproducts. The photocatalytic degradation process typically starts with the adsorption of dye molecules onto the photocatalyst surface, followed by light-induced excitation, ROS generation, and subsequent oxidation reactions. The efficacy of photocatalysts in dye degradation hinges on various performance factors, including bandgap energy, light absorption capacity, and rates of charge separation and migration. These factors directly impact the efficiency and selectivity of photocatalytic reactions. Therefore, optimizing photocatalytic performance involves enhancing both the physical adsorption capacity for dye molecules and the generation of reactive species to drive photocatalytic activity efficiently. The effectiveness of photocatalysts in dye degradation relies on their ability to adsorb dye molecules physically and initiate photocatalytic degradation processes. Balancing these aspects while considering factors such as surface morphology and chemical composition is crucial for maximizing photocatalytic performance[29].

Conclusion

In conclusion, the Fe^{3+} doped ZnO/TiO_2 photocatalyst was synthesized via the calcination method across a range of temperatures from 350 ℃ to 600 ℃, using varied proportions of compounds and solvents. The study investigated the impact of different ratios of oleic acid and $FeCl_3 \cdot 6H_2O$, various doses of the photocatalyst, and different degradation times on the photocatalytic degradation of methyl orange under both 100 W incandescent lamp and sunlight irradiation. Based on the optimization outcomes, the optimal experimental conditions were determined to achieve the photocatalyst with the highest photocatalytic efficiency. Structural characterization was performed using XRD, while SEM provided insights into the microstructure. EDS facilitated qualitative and quantitative analysis of the sample's elemental composition, and XPS was employed to measure the electron binding energy of the sample material's inner layer. The results demonstrated that the optimal ratio of Zn $(CH_3COO)_2$, $TiCl_4$, $FeCl_3 \cdot 6H_2O$, and oleic acid was 1: 1: 0.02: 3, with a calcination temperature of 400 ℃. Furthermore, the most effective dosage of the photocatalyst was determined to be 0.2 g per 100 mL of methyl orange solution. Under the irradiation of a 100 W incandescent lamp, the removal rate of methyl orange reached 90.68% after 4 h, while employing the optimal dose (0.2 g) of photocatalyst under the best conditions resulted in a concentration of 20 mg/L in 100 mL of methyl orange solution. Remarkably, under sunlight conditions, the removal rate could reach up to 97.14%. These findings indicate that the optimized Fe^{3+} doped ZnO/TiO_2 photocatalyst holds promising prospects for real-world applications, particularly in environments like wastewater treatment facilities, industrial sites emitting dye pollutants, and initiatives focused on environmental

remediation, where the efficient breakdown of organic contaminants is imperative.

Acknowledgments

This work was funded by the Fundamental Research Grant Scheme (FRGS) from Ministry of Higher Education Malaysia [Code: FRGS/1/2020/TK0/USM/02/33].

References

1 Chandanshive V, Kadam S, Rane N, Jeon B, Jadhav J & Govindwar S, In situ textile wastewater treatment in high rate transpiration system furrows planted with aquatic macrophytes and floating phytobeds, *Chemosphere*, 252 (2020) 126513.

2 Ren G, H, Wang Y, Liu S, Zhao J, Meng X & Li Z, Recent advances of photocatalytic application in water treatment: A review, *Nanomaterials*, 11 (2021) 1804.

3 Al-Tohamy R, Ali S, Fanghua L, Okasha K, Mahmoud Y, Elsamahy T, Haixin J, Yinyi F & Jianzhong S, A critical review on the treatment of dye-containing wastewater: Ecotoxicological and health concerns of textile dyes and possible remediation approaches for environmental safety, *Ecotoxicol Environ Saf*, 231 (2022) 113160.

4 Vasiljevic Z Z, Dojcinovic M P, Vujancevic J D, Jankovic-Castvan I, Ognjanovic M, Tadic N B, Stojadinovic S, Brankovic G O & Nikolic M V, Photocatalytic degradation of methylene blue under natural sunlight using iron titanate nanoparticles prepared by a modified sol-gel method, *Royal Soc Open Sci*, **7** (2020) 200708.

5 Campos-Delgado J & Mendoza M E, Ternary graphene oxide and titania nanoparticles-based nanocomposites for dye photocatalytic degradation: A Review, *Materials*, 17 (2023) 135.

6 Kumar V, Pallavi P, Sen S K & Raut S, Harnessing the potential of white rot fungi and ligninolytic enzymes for efficient textile dye degradation: A comprehensive review, *Water Environ Res*, 96 (2024) e10959.

7 Sivakumar R & Lee N Y, Emerging bismuth-based direct Z-scheme photocatalyst for the degradation of organic dye and antibiotic residues, *Chemosphere*, 297 (2022) 134227.

8 Kumari H, Sonia, Suman, Ranga R, Chahal S, Devi S,Sharma S, Kumar S, Kumar P, Kumar S, Kumar A & Parmar R, A review on photocatalysis used for wastewater treatment: Dye degradation, *Water Air Soil Pollut*, 234 (2023) 349.

9 Zielińska-Jurek Z W A, Izabela W, Piotr S & Ewa K, The effect of nanoparticles size on photocatalytic and antimicrobial properties of Ag-Pt/TiO_2 photocatalysts, *Appl Surface Sci*, 353 (2015) 317.

10 Xie G, Wei J, Hu Z & Zheng R, Preparation and photocatalytic properties of ZnO/C/TiO_2 nanoparticles, *Chin J Chem Eng*, 18 (2018) 1068.

11 Islam M, Kumar S, Saxena N& Nafees A, Photocatalytic degradation of dyes present in industrial effluents: A review, *ChemistrySelect*, 8 (2023) e202301048.

12 Haghighizadeh A, Beni A, Haghmohammadi M, Adel M & Farshad S, Green synthesis of ZnO-TiO_2 nano-photocatalyst doped with Fe(III) ions using bitter olive extract to treat textile wastewater containing reactive dyes, *Water Air Soil Pollut*, 234 (2023) 366.

13 Belver C, Hinojosa M, Bedia J, Tobajas M A, Alvarez MA, Rodríguez-González V & Rodriguez J J, Ag-coated heterostructures of ZnO-TiO_2/delaminated montmorillonite as solar photocatalysts, *Materials*, 10 (2017) 960.

14 An C W, Liu T, Zhang D F & Yan J S, Superior visible-light driven photocatalyst of Ni-doped $CdFe_2O_4$ for environmental pollutants degradation, *Kinet Catal*, 61 (2020) 854.

15 Macías-Sánchez J J, Hinojosa-Reyes L, Caballero-Quintero A, de la Cruz W, Ruiz-Ruiz E, Hernández-Ramírez A & Guzmán-Mar J L, Synthesis of nitrogen-doped ZnO by sol-gel method: Characterization and its application on visible photocatalytic degradation of 2,4-D and picloram herbicides, *Photochem Photobiol Sci*, 14 (2015) 536.

16 Huihui L, Bin L, Shu Y, Sato T & Yuhua W, Visible light-driven photocatalytic activity of oleic acid-coated TiO_2 nanoparticles synthesized from absolute ethanol solution, *Nanoscale Res Lett*, 10 (2015) 415.

17 Jingqun G, Xiaoyu L, Jun W, Baoxin W, Kai L, Ying L, Pingli K & Guangxi H, Preparation of Er^{3+}:$YAlO_3$/Fe-doped TiO_2–ZnO and its application in photocatalytic degradation of dyes under solar light irradiation, *Desalination*, 268 (2011) 68.

18 Liu L, Tang X & Chen H, Photocatalytic performance of Fe doped ZnO/TiO_2, *J Mater Sci Technol*, 40 (2022) 232.

19 Kun L, Mimérand Y, Xiaoyun J, Jungang Y & Jia G, Metal oxide (ZnO and TiO_2) and Fe-based metal-organic-framework nanoparticles on 3D-printed fractal polymer surfaces for photocatalytic degradation of organic pollutants, *ACS Appl Nano Mater*, 3 (2020) 2830.

20 Kim M G, Kang J M, Lee J E, Kim K S, Cho M & Lee S G, Effects of calcination temperature on the phase composition, photocatalytic degradation, and virucidal activities of TiO_2 nanoparticles, *ACS Omega*, 6 (2021) 10668.

21 Khan H, Habib M, Khan A &Boffito D, A modified sol-gel synthesis to yield a stable Fe^{3+}/ZnO photocatalyst: Degradation of water pollutants and mechanistic insights under UV and visible light, *J Environ Chem Eng*, 8 (2020) 104282.